ELSEVIER

Journal of Nuclear Materials 307–311 (2002) 69–73

journal of nuclear materials

www.elsevier.com/locate/jnucmat

Melt layer erosion of metallic armour targets during off-normal events in tokamaks

B. Bazylev [a,*], H. Wuerz [b]

[a] *Luikov Institute of Heat and Mass Transfer, 220072, Minsk, Belarus*
[b] *Forschungszentrum Karlsruhe, IHM, Postfach 3640, 76021 Karlsruhe, Germany*

Abstract

Melt layer erosion by melt motion is the dominating erosion mechanism for metallic armours under high heat loads. A 1-D fluid dynamics simulation model for calculation of melt motion was developed and validated against experimental results for tungsten from the e-beam facility JEBIS and beryllium from the e-beam facility JUDITH. The driving force in each case is the gradient of the surface tension. Due to the high velocity which develops in the Be melt considerable droplet splashing occurs.

1. Introduction

In ITER-FEAT tungsten is foreseen as armour material everywhere in the divertor except at the separatrix strike point (SSP) region where carbon fiber composites presently are foreseen and beryllium is foreseen as first wall (FW) armour material. During off-normal events the divertor and FW armour might experience heat loads of the GW/m^2 level. Such heat loads result in melting and evaporation [1]. Due to the rather long exposure times the melt layer thickness of the metallic armour will become several hundreds of microns. Forces acting on the melt layer induce a motion of the melted material. As a consequence of this melt layer erosion, melted material is flushed to the periphery, a rather deep erosion crater appears and at the crater edge large mountains of resolidified material are produced. Melt layer erosion will determine the lifetime of the metallic armour because of its potential to form craters hundreds of microns deep and therefore has to be analyzed carefully [2].

Forces which might cause melt layer erosion are the gradient of the total pressure above the heated surface given as a sum of the recoil pressure of the evaporating material and of the pressure of the plasma shield formed in the course of the evaporation, the gradient of the surface tension which arises because of the surface temperature gradient along the surface of the melt layer and Lorentz forces due to currents flowing in the melt layer during the heating period. For the calculation of the melt motion under the action of external forces a preliminary 1-D fluid dynamic simulation model was developed and the first results using this model were reported [3]. Meanwhile a more detailed numerical model was elaborated. The model and its validation against experimental results on melt layer erosion of tungsten samples from the electron beam facility JEBIS [4] and beryllium samples from the JUDITH facility [5] are described.

2. The 1-D fluid dynamics simulation of melt motion

Heating of the armour occurs as surface and as volumetric heating. Hot plasma impact produces surface heating, electron impact (as occurring for runaway electron impact) results in volumetric heating. Both heating scenarios have to be taken into account. In the case of a disruption heating occurs in the divertor with a characteristic heat load profile with its peak value at the

* Corresponding author. Tel.: +375-172 842485.
E-mail address: bazylev@hmti.ac.by (B. Bazylev).

0022-3115/02/$ - see front matter
PII: S0022-3115(02)00993-5

SSP. As a consequence, the external pressure and the surface tension depend on the position along the melt surface. The resulting forces due to the pressure and the surface tension gradients together with the Lorentz force act on the melt layer and might induce melt motion. In case of a VDE on the FW the heat load is relatively constant along the armour surface. Gradients of pressure and surface tension are not occurring. In this case the only external force is the Lorentz force caused by quite large Halo currents flowing into the structure [6].

For a derivation of the mathematical model for melt motion the following assumptions are used: the thickness of the melt layer is much smaller than the width of the molten layer and pressure gradients across the melt layer are absent. Therefore there exists only a velocity component parallel to the surface and a melt velocity averaged over the molten layer can be used for description of the melt motion. In this case the 'shallow water' approximation can be applied for the mathematical description of the melt motion [7,8]. The fluid is assumed to be incompressible. Temperature dependent thermo-physical data are used. The physical processes taken into account in the numerical model are: heating, melting, evaporation from the surface and resolidification, heat transport in the liquid and the solid, viscosity and melt motion by the following forces: surface tension, total external pressure, Lorentz force due to external and Eddy currents.

The melt layer and the melt motion are shown schematically in Fig. 1 for a vertical target with the SSP.

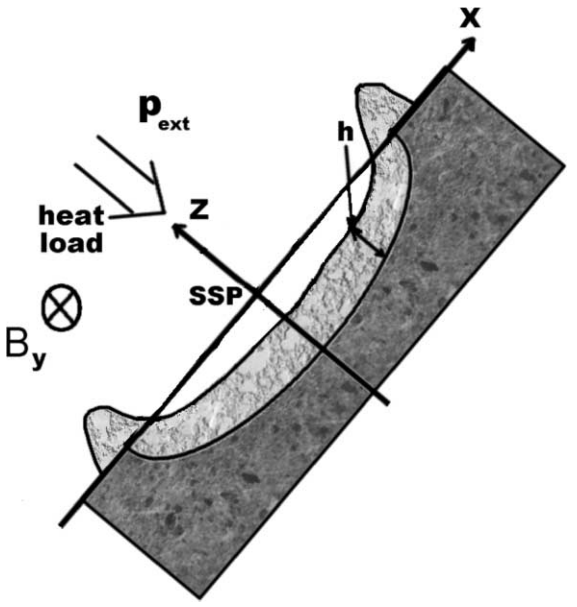

Fig. 1. Melt layer and melt motion for a vertical target schematically shown in poloidal plane, y denotes the toroidal direction.

The x-coordinate is along the surface being positive upstream from the SSP, the z-coordinate is into the layer and the y-direction is the toroidal direction, with B_y the toroidal magnetic field. The base system of Navier–Stokes equations [8] together with the heat conductivity equation describe the problem:

$$\operatorname{div} \boldsymbol{v} = 0, \tag{1}$$

$$\rho\left(\frac{\partial \boldsymbol{v}}{\partial t} + \boldsymbol{v}\nabla\boldsymbol{v}\right) = -\operatorname{grad} p + \mu\Delta\boldsymbol{v} + F_{\text{Lorentz}}, \tag{2}$$

$$\rho C\frac{\partial T}{\partial t} + \boldsymbol{v}\operatorname{grad} T = \nabla(\kappa\nabla T) + Q, \tag{3}$$

with $\boldsymbol{v}$, T, ρ, C and κ the velocity, temperature, density, specific heat and heat conductivity, μ the viscosity of the melt, and p the pressure. Q is the sum of the volumetric heating (Q_{V}), the Joule heating (Q_{J}) and the dissipation of the kinetic energy due to the viscosity (Q_μ). Q_{J} is given as $Q_{\text{J}} = J^2/\sigma$ with J the current into the sample and σ the electrical conductivity. For a potential flow Q_μ is given as $Q_\mu = \mu \operatorname{grad} v^2$ [8]. The following boundary conditions are applied at the liquid–vapor boundary:

$$-\kappa\frac{\partial T}{\partial z}\bigg|_{\text{surf}} = W(t) - \rho V_{\text{ev}}\Delta H_{\text{ev}}, \tag{4}$$

$$\mu\frac{\partial v_x}{\partial z} = \frac{\partial \alpha}{\partial x}. \tag{5}$$

In Eq. (4) the temperature gradient is calculated at the surface, $W(t)$ is the surface heat load, ΔH_{ev} the enthalpy of evaporation and V_{ev} the velocity of the evaporation front. Eq. (5) is the boundary condition for the liquid–vapor interface. It describes the balance between the forces of the gradient of the surface tension and the friction force in the liquid. v_x is the velocity component along the surface and α is the surface tension coefficient. At the melting front ($z = z_{\text{m}}$) the velocity of the melt motion is assumed to be zero and the classic Stefan boundary condition is applied to the solid–liquid interface:

$$\kappa_{\text{s}}\frac{\partial T_{\text{s}}}{\partial x}\bigg|_{z=z_{\text{m}}} - \kappa_{\text{l}}\frac{\partial T_{\text{l}}}{\partial x}\bigg|_{z=z_{\text{m}}} = \rho V_{\text{m}}\Delta H_{\text{m}}. \tag{6}$$

The index s refers to the solid and index l to the liquid phase, V_{m} is the propagation velocity of the melt front, ΔH_{m} is the enthalpy of melting.

The shallow water approximation allows to simplify the system of Eqs. (1)–(3) with the boundary conditions (4)–(6) to a system of quasi 1-D equations. The fluid velocity v is averaged over the melt layer thickness assuming a parabolic dependence. After averaging Eqs. (1) and (2) with the boundary condition (Eq. (5)) the system of equation of the St. Venant type [7] for describing the melt layer motion is obtained according to

$$\frac{\partial h}{\partial t}+\frac{1}{x^{\beta}}\frac{\partial(x^{\beta}u_x h)}{\partial x}=-V_{\mathrm{ev}}+V_{\mathrm{m}}, \tag{7}$$

$$V_{\mathrm{sf}}=-V_{\mathrm{ev}}-\frac{1}{x^{\beta}}\frac{\partial(x^{\beta}u_x h)}{\partial x}, \tag{8}$$

$$\frac{\partial u_x}{\partial t}+u_x\frac{\partial u_x}{\partial x}=-\frac{1}{\rho}\frac{\partial p}{\partial x}-\frac{u_x}{h}V_{\mathrm{m}}+\nu\frac{\partial^2 u_x}{\partial x^2}-3\nu\frac{u_x}{h^2}+\frac{3k_{\alpha}}{2\rho h}\frac{\partial T}{\partial x}+\frac{J_z B_y}{\rho c}, \tag{9}$$

with β a geometric coefficient (0 for Cartesian and 1 for cylindrical geometry), h the melt layer thickness, u_x the mean velocity of the melt layer, J_z the z component of the current into the sample, B_y the toroidal magnetic field, $\nu=\mu/\rho$ the kinematic viscosity, and $k_{\alpha}=\partial\alpha/\partial T$ with negative k_{α}. A linear dependence of the surface tension on temperature is assumed. The second term on the right-hand side of Eq. (9) describes the friction due to an increment of the fluid mass, the third and fourth terms describe effects of viscosity, the fifth term describes the effect of surface tension and the last term the volumetric Lorentz force. The second term on the left-hand side in Eq. (7) describes the velocity of the melt surface due to melt ejection. Thus the total velocity of melt surface motion V_{sf} is given by Eq. (8).

The heat conductivity equation (3) after transformation into a moving coordinate system attached to the melt layer surface splits into two equations for the solid and the liquid phase and can be written in the following form:

$$\rho C\frac{\partial T}{\partial t}=\frac{\partial}{\partial z'}\left(\kappa\frac{\partial T}{\partial z'}\right)+\rho C V_{\mathrm{sf}}\frac{\partial T}{\partial z'}+Q_{\mathrm{V}}+\frac{J^2}{\sigma}, \tag{10}$$

$$\frac{\partial T}{\partial t}+u_x\frac{\partial T}{\partial x}=\frac{3\nu}{C}\frac{u_x^2}{h^2}, \tag{11}$$

$$z'=z+\int_0^t V_{\mathrm{sf}}\,\mathrm{d}t. \tag{12}$$

The heat conductivity equation (Eq. (10)) describes the heat transfer through the liquid and the solid phase. Eq. (11) describes the heat transfer along the surface due to melt motion with the term on the right-hand side describing the viscosity heating. Eq. (12) describes the coordinate transformation into the moving coordinate system. The surface evaporation model described in [9] is used for the calculation of the evaporation process and the evaporation recoil pressure.

The system of differential equations (7), (9)–(11) with boundary conditions (4) and (6) together with Eqs. (8) and (12) describes the melt motion problem. To simplify the solution of the problem the splitting procedure is applied. In this method the full time step calculation is split into four substeps following each other and taking into account different physical processes. In the first substep the heat conductivity equation (10) with the boundary conditions (4) and (6) is solved without melt motion using an implicit numerical scheme [10]. For determining the position of the melt (resolidification) front and the velocity of its propagation, V_{m}, a special scheme with fixed time mesh and moving line of phase transition through the spatial meshes is applied [11] (in fact, the position of the phase transition front does not coincide with the mesh border and this line divides a mesh into two non-equal meshes). Because of the nonlinearity of the resulting difference equations an iteration process is used until convergence of V_{m} and of the real position of the melt front inside the meshes is achieved. In the second substep the Eqs. (7) and (8) are solved using the explicit difference method [10]. In the third substep Eq. (11) is solved using a standard explicit difference scheme and in the fourth step the surface evaporation model is applied for a determination of the evaporation and recoil vapor pressure. An analogous approach was applied for numerical simulation of laser material processing. In this case the recoil pressure of evaporation is responsible for melt motion and crater formation [12].

3. Results on melt layer erosion and discussion

3.1. JEBIS electron beam experiments with tungsten

At the e-beam facility JEBIS experiments on melt layer erosion of tungsten samples were performed using 70 keV electrons [4]. The beam impact was perpendicular to the target surface, a magnetic field was not applied. The quoted absorbed peak energy density was 2.3 MJ/m^2 with Gaussian power density profile and heat load duration of 1.8 ms. Calculated results for a tungsten sample initially at room temperature and the quoted 2.3 MJ/m^2 and 1.8 ms showed no melting, but the measured value of the crater depth was 27 μm and the residual melt layer thickness about 110 μm [13]. Increasing the heat load to 2 GW/m^2 showed melt layer erosion. Therefore, for the numerical simulation an absorbed heat load of 2 GW/m^2 was used. The dominating force responsible for melt motion in tungsten under these experimental conditions is the gradient of the surface tension. Its influence on the calculated crater depth is demonstrated in Fig. 2 for different surface tension coefficients assuming that the value of the surface tension at the melt temperature is as given in literature [14]. Assuming a k_{α} value of -9×10^{-5} N/mK the calculated crater depth is 35 μm and the residual melt layer thickness is 95 μm in good agreement with the measured value. For an initial sample temperature of 1000 °C the measured crater depth was 120 μm the

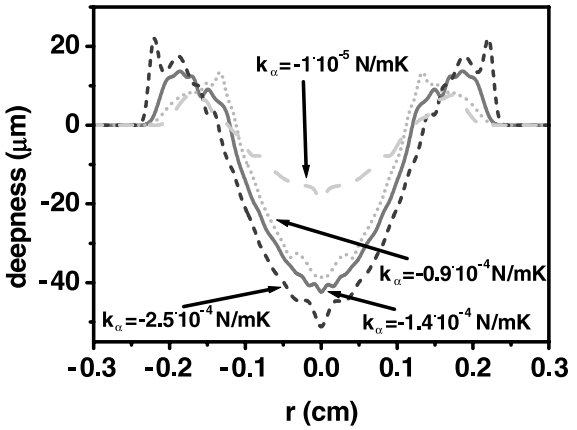

Fig. 2. Calculated crater depth of tungsten under the JEBIS experimental conditions with 2 GW/m^2 and 1.8 ms, for different coefficients of the surface tension. The initial sample temperature is room temperature.

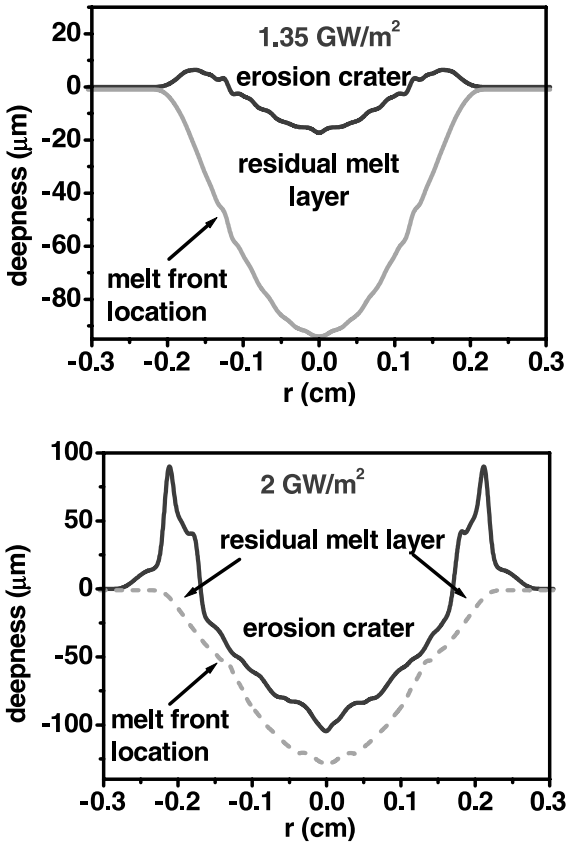

Fig. 3. Calculated results on crater depth and residual melt layer thickness of tungsten under JEBIS conditions in cylindrical geometry for the two cases with the different peak power densities of 1.3 and 2 GW/m^2. The initial sample temperature is 1000 °C, the heat load duration is 1.8 ms.

residual melt layer thickness 110 μm and the mass loss up to 2 mg. This small mass loss means that droplet splashing is rather small. Numerical results on crater depth and remaining melt layer thickness are shown in Fig. 3 for an initial sample temperature of 1000 °C for the two different absorbed energy densities 2.3 and 3.6 MJ/m^2 and using the above given k_α value. Again for 2.3 MJ/m^2 the calculated melt layer erosion values are too small. Only when increasing the heat load to 2 GW/m^2 there is reasonable agreement with the measured crater depth. From the calculated melt layer thickness of 130 μm without melt motion it is seen that the crater depth gets the size of the static melt layer. Calculated melt velocities are up to 25 cm/s. Droplet splashing due to the small melt velocity and the rather high surface tension (laminar flow of molten metal) will be rather weak in accordance with the measured rather low mass loss.

3.2. JUDITH electron beam experiments with beryllium

Fig. 4 shows experimental results on maximum crater depth in beryllium samples from the JUDITH e-beam facility with 120 keV electrons for two different experimental campaigns [5,15]. Concerning the quoted deposited energy density the results from the different experimental campaigns are not consistent. A comparison of experimental and numerical results therefore can give only indications but no final answers concerning the crater depth in the exposed beryllium. Assuming that the thermal properties of the melted and resolidified beryllium remain unchanged then the remaining residual melt layer thickness per shot is about 350 μm. Numerical results on crater depth and residual melt layer thickness are shown in Fig. 5 for a peak power density of 1.1 GW/m^2 corresponding to the lower absorbed energy density of 5 MJ/m^2 according to Fig. 4. The calculated crater depth is 220 μm and the residual melt layer thickness is 80 μm , evaporation accounts for only 5 μm. Melt

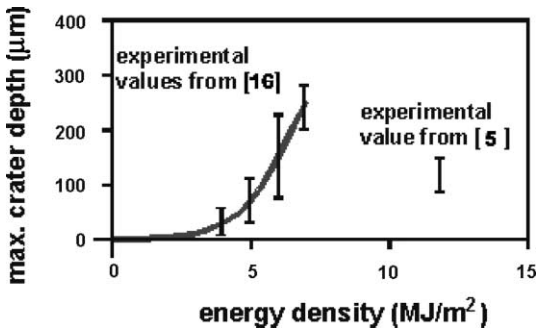

Fig. 4. Depth of the erosion crater of beryllium measured at the JUDITH facility for different absorbed energy densities. Heat load duration is 5 ms. The initial sample temperature is room temperature.

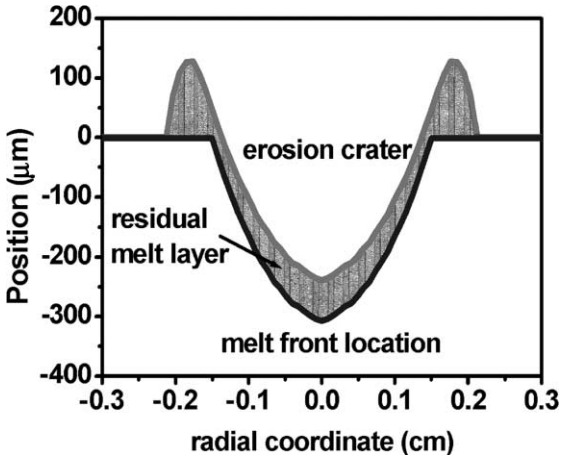

Fig. 5. Numerical results on crater depth and residual melt layer thickness of a Be sample for JUDITH with peak power density of 1.1 GW/m^2 and initial room temperature of the sample.

motion transports hot melted material to the colder periphery. As a consequence the temperature in the center of the melt drops and evaporation decreases. Therefore the experimentally determined rather large mass loss of typically 1 mg in five shots [5] corresponding to an erosion crater of about 80 μm is not caused by evaporation. The calculated velocity of the melt motion is almost up to 80 cm/s. This rather large velocity in combination with the low surface tension causes considerable droplet splashing which amounts up as much as 10% of the melted mass in these experiments. Calculated and experimental results on the crater depth of Be are in reasonable agreement only when assuming the lower value of 1.1 GW/m^2 for the peak heat load. The crater depth becomes comparable or even larger than the static melt layer thickness calculated without melt motion. The forces responsible for melt motion in beryllium are the gradient of the surface tension acting till complete resolidification which needs in these experiments 9 ms after heating stops and to a lesser extent the reactive force of the evaporating atoms which acts during the heating period. Marangoni convection flows in the melt [16] and impurities present in the sample which change the surface tension might be responsible for the considerable larger residual melt thickness in the measurement.

4. Conclusions

A 1-D fluid dynamics model for calculation of melt motion was developed and numerical results on crater depth and residual melt layer thickness were compared with experimental results for tungsten and beryllium from the e-beam facilities JEBIS and JUDITH. The crater depth in all experiments becomes comparable to the static melt layer thickness calculated without melt motion indicating that the melt layer continuously is removed by melt motion. In these experiments, because of the small size of the heated area and the absence of a magnetic field, the external force from the gradient of the surface tension is responsible for the melt motion. Qualitatively the numerical simulation describes the observed melt layer erosion. However using the heat load given in the experiment the calculated crater depth for tungsten and JEBIS conditions is too small. Reasonable agreement is only obtained when the peak energy density is increased from 2.3 to 3.6 MJ/m^2 (heat load increase from 1.3 to 2 GW/m^2). For the beryllium results at JUDITH the energy densities from different experimental campaigns are not consistent. A comparison of experimental and numerical results therefore can give only indications but no final answer concerning the crater depth in the exposed beryllium. The rather large erosion craters indicate that the use of a metallic divertor and FW armour in tokamaks under the conditions of off-normal events with high heat loads might become problematic.

References

[1] H. Wuerz et al., J. Nucl. Mater. 290–293 (2001) 1138.
[2] H. Wuerz et al., these Proceedings.
[3] H. Wuerz et al., Fus. Eng. Design 56–57 (2001) 397.
[4] K. Nakamura et al., Fus. Eng. Design 39–40 (1998) 285.
[5] A. Lodato et al., Proceedings of Fourth Workshop on Beryllium Technology for Fusion Karlsruhe Germany September 1999.
[6] ITER Physics Basis, Nucl. Fusion 39 (1999) 12.
[7] J.A. Cunge, F.M. Holly, A. Verwey, Practical Aspects of Computational River Hydraulics, Pitman, London, 1980.
[8] L.D. Landau, E.N. Lifshits, Fluid Mechanics, Pergamon, New York, 1959.
[9] S.I. Anisimov, A.Kh. Rakhmatulina, Sov. Phys. JETP 37 (1973) 441.
[10] A. Samarski, E.S Nicolaev, Numerical method for grid equations, Birkhauser, Basel, 1980.
[11] L.I. Rubinstein, The Stefan Problem, AMS, Providence, 1971.
[12] V.V. Semak, B. Damkroger, S. Kempka, J. Phys. D 32 (1999) 1819.
[13] J. Linke et al., J. Nucl. Mater. 290–293 (2001) 1102.
[14] Y.S. Touloukian (Ed.), Thermophysical Properties of Materials, Macmillan, New York, 1970.
[15] J. Linke et al., J. Nucl. Mater. 241–243 (1997) 1210.
[16] G. Tsotridis et al., Fus. Eng. Design 15 (1991) 155.